

Transition in vortex wakes of flow around an elliptic cylinder

V. L. NGUYEN^{1,2}), V. D. DUONG³), L. H. DUONG⁴)

¹) *Division of Computational Mechanics, Institute for Advanced Study in Technology, Ton Duc Thang University, Ho Chi Minh City, Vietnam, e-mail: nguyenvanluc@tdtu.edu.vn*

²) *Faculty of Civil Engineering, Ton Duc Thang University, Ho Chi Minh City, Vietnam*

³) *School of Aerospace Engineering, University of Engineering and Technology, Vietnam National University, Ha Noi City, Vietnam, e-mail: duongdv@vnu.edu.vn*

⁴) *Faculty of Engineering and Technology, Nguyen Tat Thanh University, Ho Chi Minh City, Vietnam*

TRANSITION IN THE WAKE FLOW AROUND AN ELLIPTIC CYLINDER was numerically investigated at Reynolds numbers (Re) ranging from 3 to 200. The cylinder axis ratio (AR) varies from 0.125 to 8, while its angle of attack (AoA) was examined at 30° , 60° , and 90° . Simulation results reveal the existence of eight flow patterns, such as attached flow, steady symmetric vortex flow, steady asymmetric vortex flow, Kármán vortex street, double-periodical vortex shedding, Kármán wake followed by steady shear layers, Kármán wake followed by secondary wake, and chaotic flow. These flow patterns are strongly influenced by Re , AR , and AoA . The double-periodical vortex shedding wake contains two shedding frequencies. The spatial structure analysis shows that both small and large instabilities exist significantly in this pattern, while they are trivial in the Kármán wake. The Kármán wake followed by a secondary wake is characterized by symmetric like-signed spatial structures near the cylinder and distorted ones far downstream. Meanwhile, asymmetric spatial structures of various scales contribute most energy to a chaotic flow. Root mean square of the drag coefficient is high when vortex shedding occurs for three AoA , and a notable value is observed at $AoA = 60^\circ$. Moreover, fluctuation of the lift coefficient at $AoA = 90^\circ$ is higher than those at $AoA = 30^\circ$ and 60° .

Key words: elliptic cylinder, vortex wake, vortex particle method.



Copyright © 2024 The Authors.

Published by IPPT PAN. This is an open access article under the Creative Commons Attribution License CC BY 4.0 (<https://creativecommons.org/licenses/by/4.0/>).

1. Introduction

FLOW AROUND SOLID OBSTACLES has applications in engineering industries such as heat exchangers, nuclear reactors, offshore structures, building blocks, and airplanes [1]. A comprehensive understanding of the characteristics of this flow is necessary in improving the design and controlling flow-related devices that demand high-precision dynamics. The flow passing over a cylinder in the circle

or square has been extensively studied for over a century [2] because it provides a fundamental understanding of the characteristics of the dynamics of the fluid flow around a solid obstacle. LIENHARD [3] experimentally examined the vortex wake pattern of the flow around a single circular cylinder and found that the flow is unseparated steady at the Reynolds number (Re) < 5 , steady vortex pair at $5-15 < Re < 40$, and the Kármán vortex street at $40 < Re < 200$. The flow is transitional at $200 < Re < 300$ before turning into full turbulence at $Re > 300$. Furthermore, BARKLEY and HENDERSON [4] discovered that when the Reynolds number reaches a critical value of $Re = 188$, the two-dimensional flow becomes linearly unstable to three-dimensional disturbances. BREUER *et al.* [5] numerically examined the flow around a square cylinder and reported that the steady creeping flow without separating the boundary layers on the cylinder surface exists at $Re \ll 1$. In contrast, the separation begins at the trailing edges of the cylinder to form a steady vortex pair at $Re < 5$. As Re increases, the free shear layers start to roll up to form vortices, leading to the generation of the Kármán vortex street. At a still higher Re in the range from 100 to 150, the separation occurs at the leading edges, and vortices are also generated on the upper and lower sides of the square cylinder. Thus, it is apparent that the characteristics of fluid dynamics are drastically influenced by cylinder geometry.

Flow around elliptic cylinders has also attracted much attention because it is observed in engineering applications as well as nature. For example, the antennae of seals and sea lions have elliptical cross-sections, which reduces flow-induced vibrations and thus makes it difficult for predators to detect their movement trajectory [6]. Elliptic cylinders have been widely used in industries where cooling is required, and the space is limited because elliptic cylinders have lower flow resistance and higher heat transfer than circular ones [7]. A theoretical investigation of a steady flow of a viscous fluid around an inclined elliptic cylinder at very small Re was first carried out by HASIMOTO [8] using the Oseen equations of motion. The fundamental solution for the stream function and formulas of the drag and lift coefficients were derived. KAZUHITO *et al.* [9] theoretically examined steady flows surrounding an elliptic cylinder at $Re < 1$ and showed that the Stokes flow is characterized by two singularities at two foci of the elliptic cylinder. At a higher Re , the streamline shows the presence of one or two steady vortices after the flat plate, which is considered a special case of the elliptic cylinder.

JOHNSON *et al.* [10] investigated the flow around a cylinder with its cross-section from the circle, ellipse to flat plate perpendicular to the upstream flow at $30 < Re < 200$. The study pointed out the vortex pattern is changed from the Kármán vortex street to a distinct state with the appearance of two special vortex regions. The first region is characterized by two rows of Kármán vortices shed from the ellipse and a steady flow in the middle downstream. The second

region is identified by the secondary vortex street formed by a strong interaction of Kármán vortices due to the convective instability. This instability is observed at high Re and low axis ratios (AR), and it only occurs for the flow around an elliptic cylinder. JOHNSON *et al.* [11] found the secondary and tertiary fluctuations in the region far from the cylinder by analyzing the spectrum of the vertical velocity of flow at points on the horizontal axis downstream. The energy of these frequencies is lower than that of the primary frequency near the cylinder. As Re increases and AR decreases, the energy of frequencies at the far wake becomes more significant and equals that near the cylinder. This unsteadiness of low frequency behind the flat plates is not because of the vortex interaction but two-dimensional instability.

DENNIS and YOUNG [12] and YOON *et al.* [13] investigated the steady flow around an elliptic cylinder inclined to the horizontal axis with various angles of attack α . The flow pattern is changed from the symmetric state with no separation of shear layers at $\alpha = 0^\circ$ to the asymmetric one with the separation of the shear layers to form one or two vortices. The flow then reaches a symmetric state at $\alpha = 90^\circ$ with the appearance of two vortices attached behind the cylinder. Moreover, for the steady asymmetric pattern, one vortex is attached to the cylinder surface while the rest is not. FARUQUEE *et al.* [1] studied the influence of AR of the elliptic cylinder on the formation of a pair of steady vortices. The research showed that $AR = 0.34$ is the threshold value to switch the Stokes flow into that composed of two steady vortices. Then, PAUL *et al.* [14] generalized threshold values of Re to convert the Stokes to the separation flows, the steady to the unsteady flows, and the Strouhal number corresponding to these unsteady flows. SHI *et al.* [2] numerically investigated the flow around an elliptic cylinder at $Re = 150$ and found three flow patterns such as steady wake with $AR < 0.37$ and $\alpha < 2.5^\circ$, the Kármán wake followed by a steady wake with $AR \geq 0.37-0.67$, and the Kármán wake followed by a secondary wake with $AR < 0.67$ and $\alpha > 52^\circ$. For the secondary pattern, the Kármán vortex street is formed behind the cylinder, and these Kármán vortices decay as moving downstream, resulting in the generation of two steady shear layers. For the third pattern, these two steady shear layers roll up to form a secondary vortex street of a lower frequency.

Based on the literature reviewed above, it is seen that several research works have been devoted to expanding the knowledge of the characteristics of the flow around an elliptic cylinder. However, a comprehensive understanding of the vortex wake of this flow has not been given. The above-mentioned research works offered a sparseness of flow patterns with the narrow ranges of the Reynolds number, the axis ratio, and the angle of attack of the elliptic cylinder. HASIMOTO [8], KAZUHITO *et al.* [9], DENNIS and YOUNG [12], YOON *et al.* [13], and FARUQUEE *et al.* [1] focused on the steady flow patterns rather than the unsteady ones. JOHNSON *et al.* [10, 11] investigated the effects of the cylinder shape from

the circle, ellipse to flat plate perpendicular to the upstream flow on the wake pattern at $30 \leq \text{Re} \leq 200$. However, the flow patterns behind a long elliptic cylinder were not examined. PAUL *et al.* [14] concentrated on the threshold values of Re for the transition between Stokes and separated flows, the steady and unsteady flows. Meanwhile, the vortex wake structure of the flow far downstream was not discussed. SHI *et al.* [2] studied the flow pattern around an elliptic cylinder at only Re of 150, while the important remaining range of Re for the laminar flow was not considered. Hence, this study continues shedding some light on the characteristics of the vortex wake pattern of the flow around an elliptic cylinder with large ranges of Re , AR , and angle of attack. We point out that some novel flow patterns can exist at a certain Re , the axis ratio AR , and the angle of attack of the cylinder α , such as double vortex shedding and chaotic flow. The vortex wake behind an elliptic cylinder is classified into eight patterns based on Re , AR , and the angle of attack. They are identified based on the characteristics of the vortex shedding from the cylinder and the structure of the vortex wake of the vorticity contour, streamlines, and energy spectrum of the lift coefficient. The deterministic spatial structures of these patterns are analyzed using the proper orthogonal decomposition technique. This analysis allows further insight into the deterministic spatial structures of vortex wakes behind an elliptic cylinder that previous studies have not clarified yet. We map flow patterns, drag coefficient, vortex shedding frequency, and force fluctuation based on three flow parameters (Re , AR , and the angle of attack). Therefore, the results of this study provide a comprehensive understanding of the characteristics of flow around an elliptic cylinder. The rest of the paper is organized as follows: the numerical method and its validation are described in Section 2, the characteristics of the vortex wake of the flow around an elliptic cylinder are discussed in Section 3, and the conclusions are finally given in Section 4.

2. Numerical method

The continuity and momentum velocity-pressure Navier–Stokes equations for the flow of an incompressible viscous fluid are written in the penalization term to express the appearance of the solid body as

$$(2.1) \quad \nabla \cdot \mathbf{u} = 0,$$

$$(2.2) \quad \frac{\partial \mathbf{u}}{\partial t} + (\mathbf{u} \cdot \nabla) \mathbf{u} = -\frac{1}{\rho} \nabla p + \nu \nabla^2 \mathbf{u} + \mathbf{g} + \lambda \chi_s (\mathbf{u}_s - \mathbf{u}),$$

where $\mathbf{u}(\mathbf{x}, t)$ is the velocity field, \mathbf{x} is the space coordinate, t is the time, ρ is the fluid density, p is the pressure, ν is the kinematic viscosity, and \mathbf{g} is the gravitational acceleration, \mathbf{u}_s stands for the solid velocity, λ is the penalization

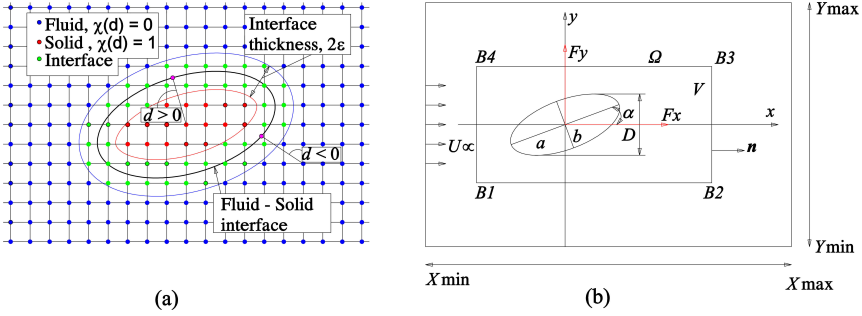


FIG. 1. (a) Configuration of solid and fluid domains; (b) Sketch of position and oblique direction of an elliptic cylinder in the Cartesian coordinate system (Oxy) and rectangular control volume ($B_1B_2B_3B_4$) used to compute the force components (F_x and F_y). The major and minor axes of the elliptic cylinder are a and b , and the axis ratio is defined as $AR = b/a$. The cylinder is placed at the angle of attack α -degree regarding the horizontal axis. D is the characteristic length, and it is determined as the projection of the elliptic cylinder on the y -axis.

parameter, and χ identifies the solid and fluid regions ($\chi(\mathbf{x}) = 0, 1$ if $\mathbf{x} \in$ fluid and solid domains, respectively, as shown in Fig. 1(a)). Equation (2.2) can be expressed in the vorticity-velocity form by applying the curl operation on both its sides as

$$(2.3) \quad \frac{\partial \boldsymbol{\omega}}{\partial t} + (\mathbf{u} \cdot \nabla) \boldsymbol{\omega} = \nu \nabla^2 \boldsymbol{\omega} + (\boldsymbol{\omega} \cdot \nabla) \mathbf{u} + \nabla \times (\lambda \chi_s (\mathbf{u}_s - \mathbf{u})),$$

where the vorticity is defined as $\boldsymbol{\omega} = \nabla \times \mathbf{u}$. The vortex particle method describes the fluid motion using the Lagrangian reference frame and computes the flow momentum using the Eulerian transport equation. The fluid is discretized into the vortex particles in the Lagrangian specification, which move at the local flow velocity and transport the flow momentum in vorticity. The momentum equation, Eq. (2.3), can be written in the Lagrangian reference frame of the vortex particles p transporting their vorticity field $\boldsymbol{\omega}(\mathbf{x}_p)$ as

$$(2.4) \quad \frac{d\mathbf{x}_p}{dt} = \mathbf{u}(\mathbf{x}_p),$$

$$(2.5) \quad \frac{d\boldsymbol{\omega}(\mathbf{x}_p)}{dt} = \nu \nabla^2 \boldsymbol{\omega}(\mathbf{x}_p) + (\boldsymbol{\omega}(\mathbf{x}_p) \cdot \nabla) \mathbf{u}(\mathbf{x}_p) + \nabla \times [\lambda \chi_s (\mathbf{u}_s(\mathbf{x}_p) - \mathbf{u}(\mathbf{x}_p))].$$

The velocity field in Eqs. (2.4) and (2.5) can be decomposed into irrotational and rotational vector fields by using the Helmholtz theorem as

$$(2.6) \quad \mathbf{u} = \nabla \phi + \nabla \times \boldsymbol{\psi},$$

where the vector $\boldsymbol{\psi}$ and scalar ϕ potentials of the velocity field are computed through solving the Poisson and Laplace equations as

$$(2.7) \quad \nabla^2 \boldsymbol{\psi} = -\boldsymbol{\omega},$$

$$(2.8) \quad \nabla^2 \phi = 0.$$

These equations are derived by taking the curl and divergence operations on both sides of Eq. (2.6). The vortex particles are initially settled on the regular grid nodes, and the change in their vorticity $\boldsymbol{\omega}(\mathbf{x}_p)$ is estimated using Eq. (2.5). These particles move to the Lagrangian locations (\mathbf{x}_p) due to their convection (Eq. (2.4)). They are then redistributed onto the initial mesh with their vorticity interpolated from that at the Lagrangian location \mathbf{x}_p as

$$(2.9) \quad \boldsymbol{\omega}(\mathbf{x}_q) = \sum_p^{n_p} \boldsymbol{\omega}(\mathbf{x}_p) W\left(\frac{x_q - x_p}{\Delta x}\right) W\left(\frac{y_q - y_p}{\Delta y}\right),$$

where $\mathbf{x}_q = (x_q, y_q)$ is the grid location, and $\mathbf{x}_p = (x_p, y_p)$ is the Lagrangian location, Δx and Δy are grid cell sizes in the x and y directions, n_p is the vortex particle number, and the third-order accuracy kernel-interpolation function $W(x)$ [15] is expressed as

$$(2.10) \quad W(x) = \begin{cases} 1 - 2.5|x|^2 + 1.5|x|^3 & \text{if } |x| \leq 1, \\ 0.5(2 - |x|)^2(1 - |x|) & \text{if } 1 < |x| \leq 2, \\ 0 & \text{if } |x| > 2. \end{cases}$$

The $W(x)$ conserves the following flow momentum [16],

$$M_0 = \int_{\Omega} \boldsymbol{\omega} d\Omega, \quad M_1 = \frac{1}{2} \int_{\Omega} \mathbf{x} \times \boldsymbol{\omega} d\Omega, \quad M_2 = \frac{1}{3} \int_{\Omega} \mathbf{x} \times (\mathbf{x} \times \boldsymbol{\omega}) d\Omega.$$

Given an elliptic cylinder immersed in a fluid flow as shown in Fig. 1(b), the drag (Cd) and lift (Cl) coefficients of the flow acting on the cylinder are expressed as $Cd = 2Fx/\rho DU_{\infty}^2$ and $Cl = 2Fy/\rho DU_{\infty}^2$. The force components Fx and Fy are derived from the control volume formula of NOCA *et al.* [17] and further expressed in the previous research work [18].

The convergence study and the validation of the current numerical method are carried out using benchmark simulations of the flow around a single circular cylinder at Re of 100 and 200. The computational domain $(-7D, 68D) \times (-7.5D, 7.5D)$ is discretized into cubic grid cells. The non-dimensional time step ($\Delta t^* = U_{\infty} t/D$) is set as 0.0025. Table 1 shows the convergence of simulation results of the flow around a cylinder at Re = 200 using four grid resolutions. It is transparent that Cda and St are convergent with the decrease in the grid

cell size, while this is not observed for Clm at $\Delta x = 0.02D$, $0.015D$, and $0.01D$. However, this aspect can be acceptable because the amplitude of the lift force oscillation fluctuates slightly around the expected value at the finest grid resolution ($\Delta x = 0.01D$). This indicates the consistency of the numerical method developed to simulate the laminar flow around a solid body.

TABLE 1. A convergence study: The time-averaged drag coefficient (Cda) and maximal lift coefficient (Clm) and Strouhal number (St) of the vortex shedding of the flow over a single circular cylinder at $Re = 200$ obtained using four grid resolutions.

$\Delta x = \Delta y$	$0.025D$	$0.02D$	$0.015D$	$0.01D$
Cda	1.458	1.436	1.409	1.375
Clm	± 0.75	± 0.89	± 0.875	± 0.874
St	0.185	0.19	0.19	0.195

Table 2 shows a comparison of the present simulation results of Cda , Clm , and St of the flow around a circular cylinder at Re of 100 and 200 with the existing results. At $Re = 100$, Cda obtained by the present simulation has a slight difference from the simulation results provided by MIMÉAU *et al.* [24]. However, it agrees well with the simulation results given by SHARMAN *et al.* [19], DING *et al.* [20], CHOI *et al.* [21], HARICHANDAN and ROY [22], SUPRADEEPAN and ROY [23], DUONG *et al.* [25] and FIRDAUS *et al.* [26]. Although the Clm gained by the present simulation is higher than those by HARICHANDAN and ROY [22], SUPRADEEPAN and ROY [23], and DUNG *et al.* [25], it matches well with the rest of the research works [20, 21, 24, 26]. The St at this Re compares favorably to existing simulation results. Similarly, Cda , Clm , and St at $Re = 200$

TABLE 2. A comparison of the time-averaged drag coefficient (Cda), the maximal lift coefficient (Clm), and the Strouhal number (St) of the vortex shedding of the flow around a single circular cylinder at Re of 100 and 200.

Authors	Re = 100			Re = 200		
	Cda	Clm	St	Cda	Clm	St
Present authors	1.365 ± 0.01	0 ± 0.33	0.16	1.375 ± 0.06	0 ± 0.874	0.195
SHARMAN <i>et al.</i> [19]	1.330 ± 0.0064	0 ± 0.230	0.164	–	–	–
DING <i>et al.</i> [20]	1.356 ± 0.010	0 ± 0.287	0.166	1.348 ± 0.050	0 ± 0.659	0.196
CHOI <i>et al.</i> [21]	1.340 ± 0.011	0 ± 0.315	0.164	1.360 ± 0.048	0 ± 0.640	0.191
HARICHANDAN and ROY [22]	1.350 ± 0.010	0 ± 0.278	0.161	1.32 ± 0.05	0 ± 0.602	0.192
SUPRADEEPAN and ROY [23]	1.36 ± 0.01	0 ± 0.275	0.161	1.42 ± 0.05	0 ± 0.652	0.198
MIMÉAU <i>et al.</i> [24]	1.4 ± 0.01	0 ± 0.32	0.165	1.44 ± 0.05	0 ± 0.75	0.2
DUNG <i>et al.</i> [25]	1.335	0 ± 0.221	0.168	1.325	0 ± 0.475	0.201
FIRDAUS <i>et al.</i> [26]	1.351	0 ± 0.351	0.172	1.367	0 ± 0.734	0.208

by the present simulation correlate well with the existing literature results. Thus, the present numerical method can well capture the characteristics of laminar flow around a bluff solid body.

3. Wake pattern of the flow around an elliptic cylinder

This section sheds some light on the characteristics of the laminar flow around an elliptic cylinder at Re ranging from 3 to 200. The effects of the elliptic cylinder's axis ratio (AR) and its angle of attack (α) regarding the horizontal axis, as sketched in Fig. 1(b), on the wake pattern are also clarified. AR varies from 0.125 to 8, while α is investigated at 30° , 60° , and 90° .

3.1. Steady flows

Figure 2 shows streamlines of the flow around an elliptic cylinder with its AR ranging from 0.125 to 8 at $\alpha = 30^\circ$, 60° and 90° at $Re = 3$. It is observed that

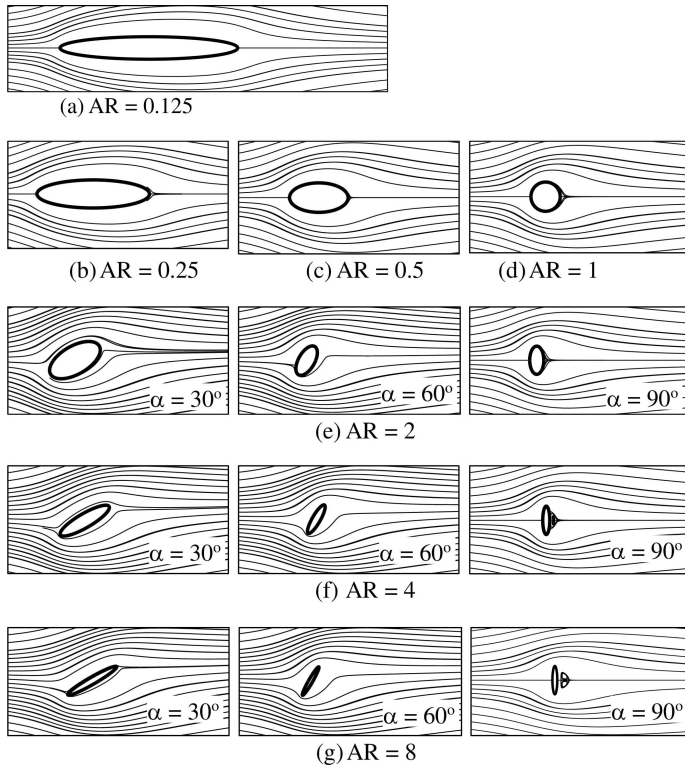


FIG. 2. Streamlines of the flow around an elliptic cylinder at $\alpha = 30^\circ$, 60° and 90° at $Re = 3$ with its (a) AR = 0.125, (b) AR = 0.25, (c) AR = 0.5, (d) AR = 1, (e) AR = 2, (f) AR = 4, and (g) AR = 8.

except for the cases of $AR = 4$ and 8 with $\alpha = 90^\circ$, the steady shear layers of the flow attach to the cylinder surface, and the separation does not occur. This pattern is named attached flow. The flow streamlines attach to the body surface more favorably at a lower α and/or a lower AR .

For $AR = 4$ and 8 with $\alpha = 90^\circ$, as shown in the third column of Figs. 2(f) and 2(g), a steady symmetric vortex pair flow is observed. The boundary layers are generated on the cylinder surface and separate from both sides at certain points. They then roll up to form a counting-rotating vortex pair behind the cylinder. This vortex pair does not lose its stability due to a weak flow at this Re , and its position remains unchanged for the whole time evolution. The size of the vortex pair grows as AR increases. This is explained by the fact that the recirculation zone behind the cylinder at a higher AR is larger than at a lower AR . Therefore, the vortices behind the cylinder develop in greater size at a higher AR . Moreover, we also investigated the wake pattern of the flow around the elliptic cylinder at $AR = 4$ and 8 with $\alpha = 90^\circ$ at a lower Re and found that the ‘attacked flow’ occurs at $Re = 2$.

Figure 3 expresses the time evolution of Cd of the attached flow and the steady symmetric vortex pair flow exerted on the cylinder at $Re = 3$. Note that

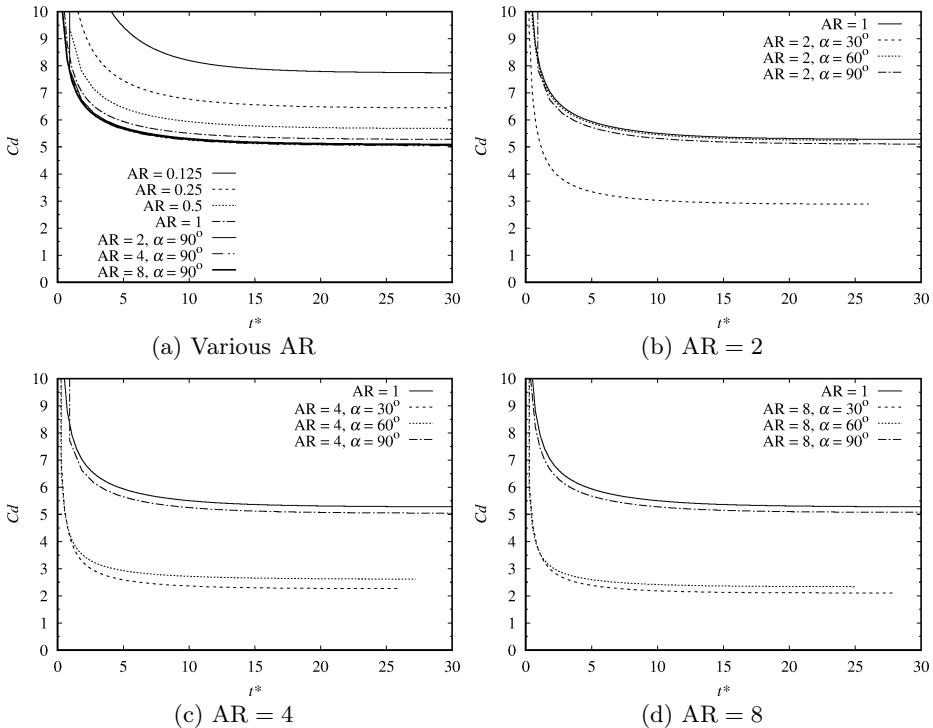


FIG. 3. Time evolution of Cd of the flow exerted on an elliptic cylinder at (a) $Re = 3$ with various axis ratios, (b) $AR = 2$, (c) $AR = 4$, and (d) $AR = 8$.

the fluid force of the flow acting on the cylinder can be decomposed into skin friction and pressure components. The first component, expressing the effects of the fluid viscosity, plays a dominant role at a low Re , while the second recovers its importance as Re increases. Due to steady flows, Cd does not fluctuate and remains unchanged after the early stage of the flow. Cd drastically decreases as AR increases from 0.125 to 1, as observed in Fig. 3(a). This is explained by the fact that the surface area of the cylinder immersed in the fluid is greater at a lower AR , leading to higher skin friction drag. Cd slightly reduces as AR varies from 1 to 8 due to a trivial change in the wetted area of the elliptic cylinder. At $AR = 2$, as shown in Fig. 3(b), Cd at $\alpha = 60^\circ$ and 90° is slightly lower than that of the flow around a circular cylinder ($AR = 1$). Cd at $\alpha = 30^\circ$ drastically reduces because the streamlines of flow have smoother paths surrounding the solid body; hence, the resistance to flow is lower. At $AR = 4$ and 8, as seen in Fig. 3(c) and Fig. 3(d), Cd at $\alpha = 90^\circ$ slightly decreases compared to that at $AR = 1$, while a significant reduction is observed at $\alpha = 30^\circ$ and 60° .

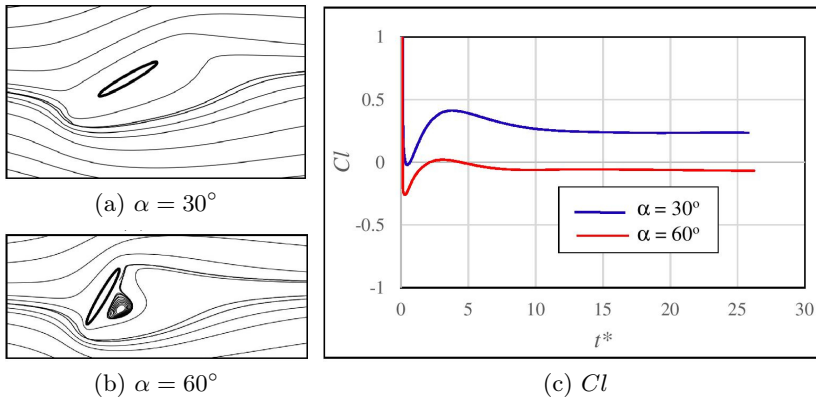


FIG. 4. Streamlines of the flow around an elliptic cylinder with $AR = 8$ at $Re = 10$: (a) $\alpha = 30^\circ$, (b) $\alpha = 60^\circ$, (c) the lift coefficients of the flow exerted on the cylinder at these α .

Figure 4 depicts the instantaneous streamline and the temporal evolution of the lift coefficient of flow exerted on an elliptic cylinder with $AR = 8$ at $\alpha = 30^\circ$ and 60° at $Re = 10$. The flow is steady at this Re for both α , as demonstrated in the plots of Cl in Fig. 4(c). The attached flow appears at $\alpha = 30^\circ$, while a steady vortex is generated behind the cylinder at $\alpha = 60^\circ$. This flow pattern is named steady asymmetric vortex flow.

3.2. Double-periodical vortex shedding

Figure 5 shows streamlines of the flow around an elliptic cylinder at $Re = 40$. The attached flow takes place at $AR = 0.125$, as seen in Fig. 5(a), while the

steady symmetric vortex pair flow is observed at $AR = 0.25, 0.5, 1$ and $AR = 2, 4, 8$ with $\alpha = 90^\circ$, as manifested in Figs. 5(b–g).

For $AR = 2, 4,$ and 8 with $\alpha = 30^\circ$, as shown in the first column of Fig. 5, the vortices are alternately equally shed from one side to another of the elliptic cylinder and form a Kármán vortex street downstream, as further evidenced in plots of vorticity contours shown in Figs. 6(a), 6(c) and 6(e). This flow is switched from the steady symmetric vortex pair flow. The Re for this pattern is higher than that of the steady symmetric vortex pair flow.

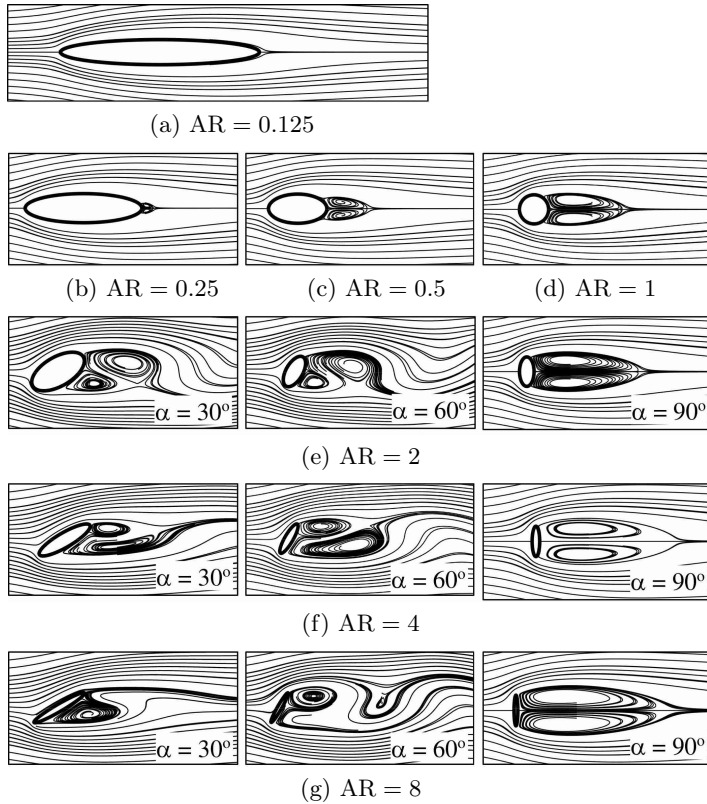


FIG. 5. Streamlines of the flow around an elliptic cylinder with its various AR and α at $Re = 40$: (a) $AR = 0.125$, (b) $AR = 0.25$, (c) $AR = 0.5$, (d) $AR = 1$, (e) $AR = 2$, (f) $AR = 4$, and (g) $AR = 8$.

For $AR = 2, 4,$ and 8 with $\alpha = 60^\circ$, as shown in the second column of Fig. 5, the vortices are also shed from both sides of the cylinder. The vortex wake is similar to that of a Kármán vortex street, as seen in Figs. 6(b), 6(d) and 6(f). However, the frequency of the vortex shedding from two sides of the elliptic cylinder differs, compared to the Kármán vortex shedding. Two periodical vortex sheddings are formed, as given later evidence; therefore, this pattern is

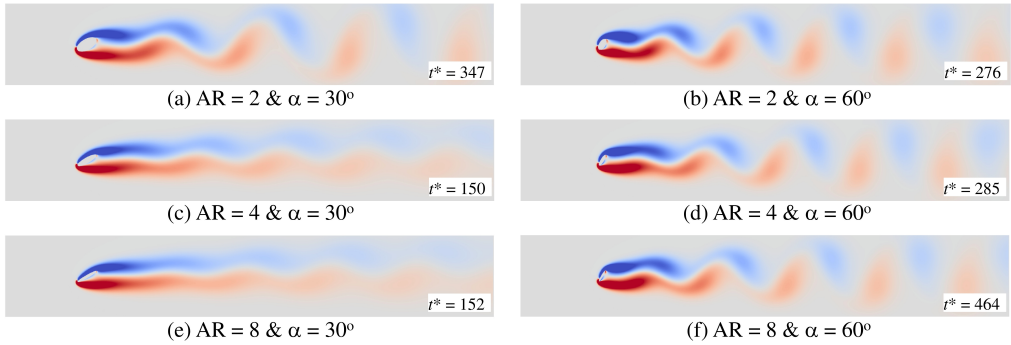


FIG. 6. Instantaneous distribution of the vorticity of the flow around an elliptic cylinder with its various AR and α at $Re = 40$: (a) $AR = 2$ & $\alpha = 30^\circ$, (b) $AR = 2$ & $\alpha = 60^\circ$, (c) $AR = 4$ & $\alpha = 30^\circ$, (d) $AR = 4$ & $\alpha = 60^\circ$, (e) $AR = 8$ & $\alpha = 30^\circ$, and (f) $AR = 8$ & $\alpha = 60^\circ$.

named double-periodical vortex shedding. This flow pattern is for the first time reported in this research. This flow pattern is only observed at high AR of 2, 4, and 8 at $\alpha = 60^\circ$, and it does not take place at $AR \leq 1$.

Figure 7 exhibits the time evolution of Cd of the attached flow and the steady symmetric vortex pair flow exerted on an elliptic cylinder with its various AR at $Re = 40$. As AR increases from 0.125 to 0.5, Cd significantly decreases because of a remarkable reduction in the skin friction force. The behavior of Cd at this Re is similar to that at $Re = 3$. However, the intensity of the change at this Re is lower than that at $Re = 3$. This is because the effects of the viscous force decrease while the pressure component increases at a higher Re . Cd gradually increases when AR rises from 0.5 to 8. This can be explained by the fact that at a higher AR, the region of the reserve flow is larger, leading to a greater gradient of pressure on the front and back surfaces of the cylinder.

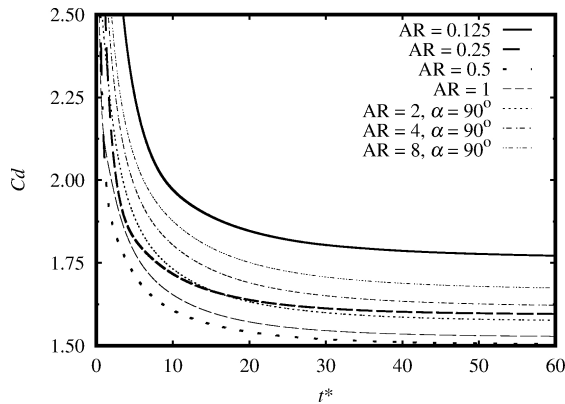


FIG. 7. Time evolution of Cd of the ‘attached flow’ and the ‘steady symmetric vortex pair flow’ exerted on an elliptic cylinder with its various AR at $Re = 40$.

Figures 8(a) and 8(b) describe the time evolution of Cd and Cl of the Kármán vortex street flow acting on an elliptic cylinder with its various AR of 2, 4 and 8 at $\alpha = 30^\circ$ at $Re = 40$. They periodically fluctuate with time, and the maximal oscillation amplitude belongs to the case with $AR = 2$, followed by $AR = 4$ and 8. This is explained by the fact that the vortices generated behind the cylinder at $AR = 2$ are more robust than $AR = 4$ and 8, as seen in plots of streamlines shown in Figs. 5(e) and 5(f), resulting in a greater flow impact on the cylinder.

Figures 8(c) and 8(d) show the time evolution of Cd and Cl of the flow exerted on an elliptic cylinder with its AR of 2, 4, and 8 at $\alpha = 60^\circ$ at $Re = 40$. The behavior of Cd and Cl in this pattern is different from that of the Kármán vortex street one. We used the case of $AR = 8$ and $\alpha = 60^\circ$ to represent others with the same flow characteristics and analyzed the frequency of Cl . The Strouhal number of vortex shedding at the upper and lower separation points are respectively measured as 0.11 and 0.12. The vortex shedding at the lower edge takes place more slowly than from the upper one. This is explained by the fact that the

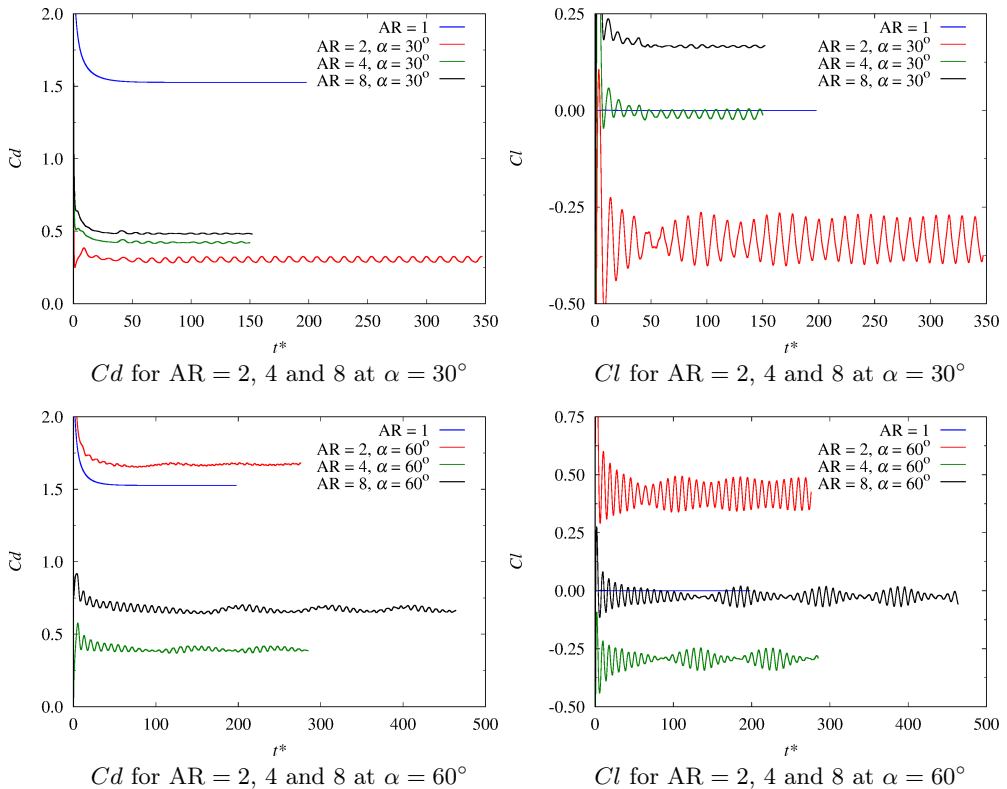


FIG. 8. Time evolution of Cd and Cl of the flow exerted on an elliptic cylinder with its various AR at $\alpha = 30^\circ$ and 60° at $Re = 40$.

recirculation region near the lower separation point is larger than the upper one. The time of vortex development near the lower separation point lasts longer than that near the upper one.

3.3. Kármán wake followed by steady shear layers

Figure 9 shows the instantaneous distribution of the vorticity field of the flow around an elliptic cylinder with its various AR at $\alpha = 30^\circ$, 60° and 90° and $Re = 65$. The attached flow still takes place at $AR = 0.125$, while the steady symmetric vortex pair flow is observed at $AR = 0.25$ and 0.5 . The plots of streamlines for these simulation cases, as presented in Figs. 10(a), 10(e) and 10(f), further demonstrate these flow patterns. For the simulation cases with $AR = 1$, $AR = 2$ ($\alpha = 30^\circ$, 60° and 90°), $AR = 4$ ($\alpha = 30^\circ$ and 60°), $AR = 8$ ($\alpha = 30^\circ$ and 60°), the Kármán vortex street is formed behind the elliptic cylinder.

For $AR = 4$ and 8 with their $\alpha = 90^\circ$, as seen in the third column of Figs. 9(f) and 9(g), the Kármán vortices are observed behind the cylinder; however, these vortices rapidly decay as moving far from the cylinder. The merging of these vortices forms two steady shear layers. Therefore, this flow pattern is named Kármán wake followed by steady shear layers.

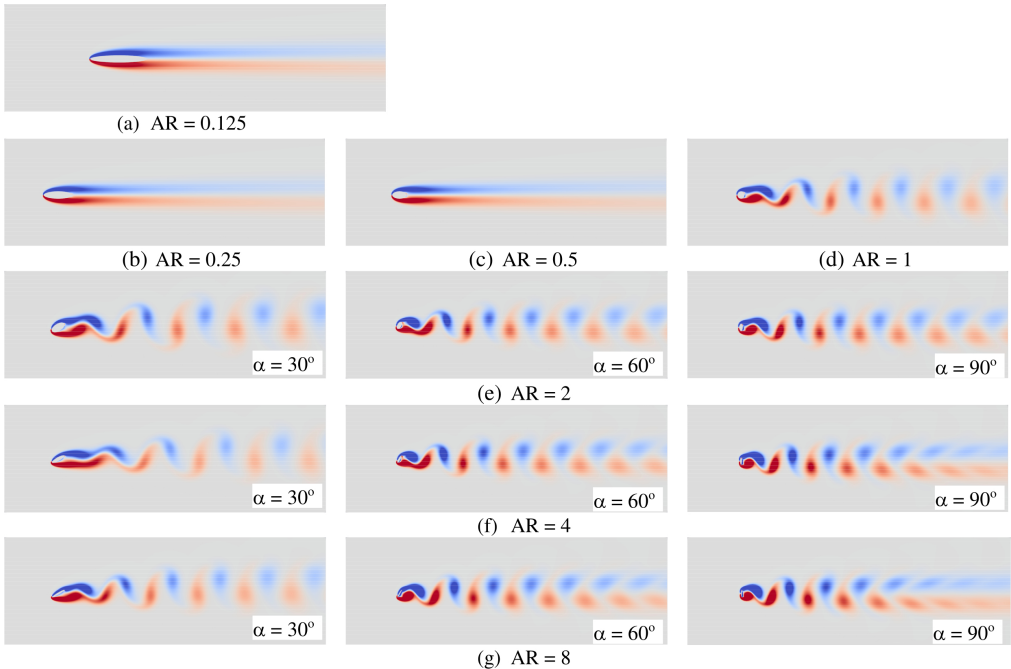


FIG. 9. Instantaneous distribution of the vorticity field of the flow around an elliptic cylinder with its various AR and α at $Re = 65$: (a) $AR = 0.125$, (b) $AR = 0.25$, (c) $AR = 0.5$, (d) $AR = 1$, (e) $AR = 2$, (f) $AR = 4$, and (g) $AR = 8$.

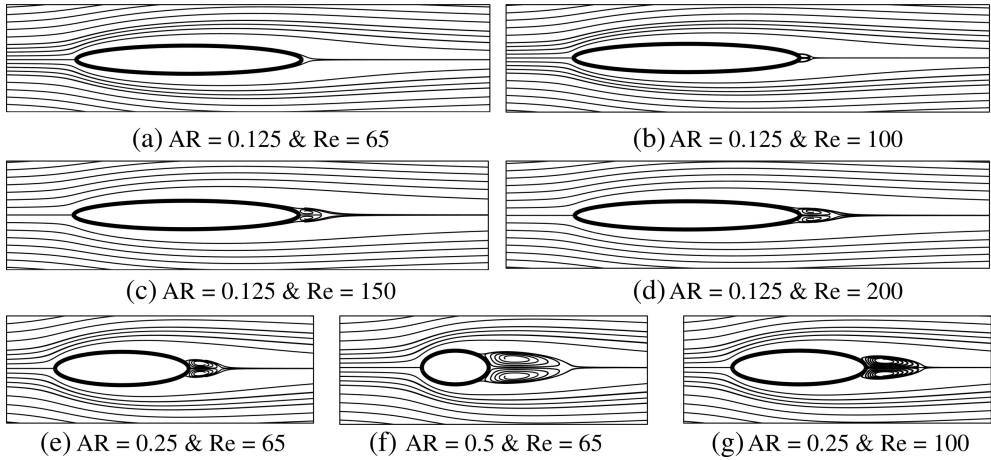


FIG. 10. Instantaneous distribution of the vorticity field of the flow around an elliptic cylinder with its various AR and Re: (a) AR = 0.125 and Re = 65, (b) AR = 0.125 and Re = 100, (c) AR = 0.125 and Re = 150, (d) AR = 0.125 and Re = 200, (e) AR = 0.25 and Re = 65, (f) AR = 0.5 and Re = 65, and (g) AR = 0.25 and Re = 100.

Figure 11 describes the time evolution of Cd of the flow acting on an elliptic cylinder at $Re = 65$. For $AR = 0.125, 0.25$, and 0.5 , the flow is steady, and Cd approaches a constant value after a short early stage of the flow, as shown in Fig. 11(a). This drag coefficient reduces as AR increases due to a decrease in the skin friction force. For $AR = 1$, the Kármán vortex street occurs; therefore, Cd fluctuates periodically, and its time-averaged value is higher than those at $AR = 0.125, 0.25$, and 0.5 . For $AR = 2, 4$, and 8 , as shown in Figs. 11(b–d), Cd also fluctuates periodically. This demonstrates that the Kármán vortex street or Kármán wake followed by steady shear layers are features of these flows. The fluctuation amplitudes of Cds at these AR are higher than that at $AR = 1$, and the vortex shedding occurs more strongly.

At $\alpha = 30^\circ$, as shown in Fig. 11(b), the time-averaged value of Cd significantly increases as the axis ratio increases from $AR = 2$ to 8 . This is because of an increase in the gradient of the forward and reverse pressures from the front and back surfaces of the cylinder, as previously discussed. At a higher AR, the region for reverse pressure is larger, so the pressure gradient between the front and back surfaces is greater. Cds at $AR = 2, 4$, and 8 are lower than that at $AR = 1$ because the fluid flow surrounding the cylinder at $\alpha = 30^\circ$ is smoother than that at $AR = 1$. At $\alpha = 60^\circ$, as shown in Fig. 11(c), the fluctuation intensity of Cd is strong at $AR = 4$ and 8 , followed by that at $AR = 2$. The Kármán vortices are robustly formed at this angle of attack, leading to their conservation far downstream. At $\alpha = 90^\circ$, as shown in Fig. 11(d), an increase in Cd from $AR = 2$ to 8 is also observed, and Cds at these AR are higher than at

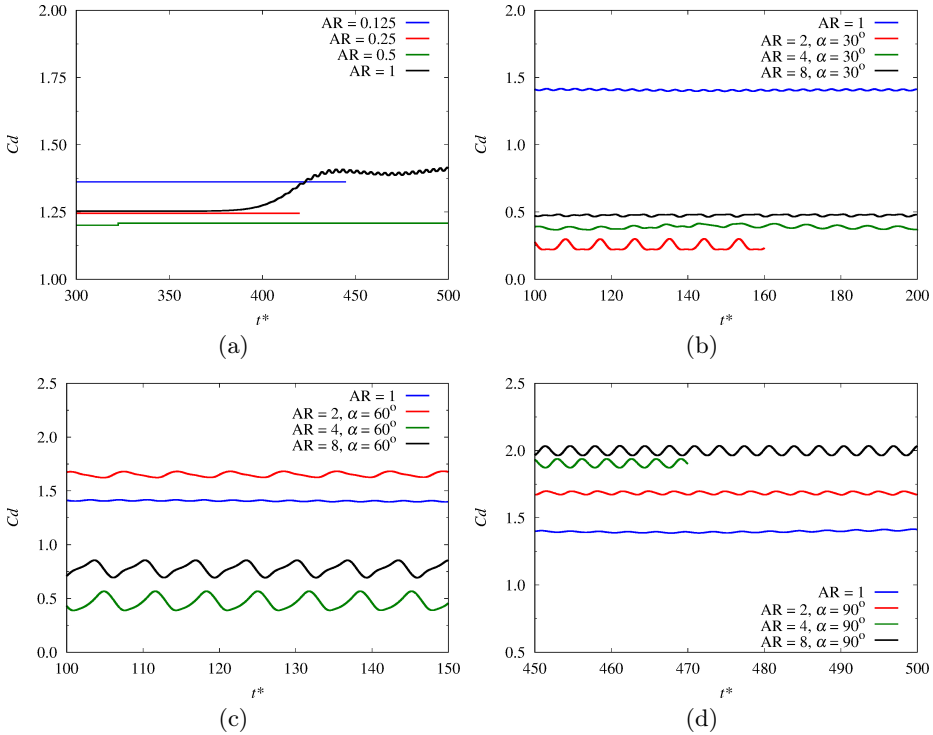


FIG. 11. Time evolution of C_d of the flow exerted on an elliptic cylinder with its various AR and α at $Re = 65$: (a) $AR = 0.125, 0.25, 0.5$, and 1 , (b) $AR = 2, 4$, and 8 at $\alpha = 30^\circ$, (c) $AR = 2, 4$, and 8 at $\alpha = 60^\circ$, and (d) $AR = 2, 4$, and 8 at $\alpha = 90^\circ$.

$AR = 1$. This indicates that the resistance to the flow by a solid body as a flat plate perpendicular to the flow is higher than that around a circular cylinder.

3.4. Kármán wake followed by a secondary wake

Figure 12 shows an instantaneous distribution of the vorticity field of the flow around an elliptic cylinder at $Re = 100$. The steady symmetric vortex pair flow takes place at $AR = 0.125$ and 0.25 , as further proved using plots of streamlines in Figs. 10(b) and 10(g). The Kármán vortex street is formed downstream for the cases of $AR = 0.5, 1$, and $AR = 2, 4$, and 8 with their $\alpha = 30^\circ$, as seen in the first column in Figs. 12(d–g). For $AR = 2$ with $\alpha = 60^\circ, 90^\circ$, the Kármán wake followed by steady shear layers is observed. For $AR = 4, 8$ with $\alpha = 60^\circ, 90^\circ$, as shown in the second and third columns in Figs. 12(f, g), the Kármán vortices are formed, and these vortices also merge to generate two steady shear layers in the middle region downstream. Due to convective instability, these shear layers roll up to form larger-scale counter-rotating vortices, resulting in a secondary wake. Hence, this flow pattern is named Kármán wake followed by the secondary wake.

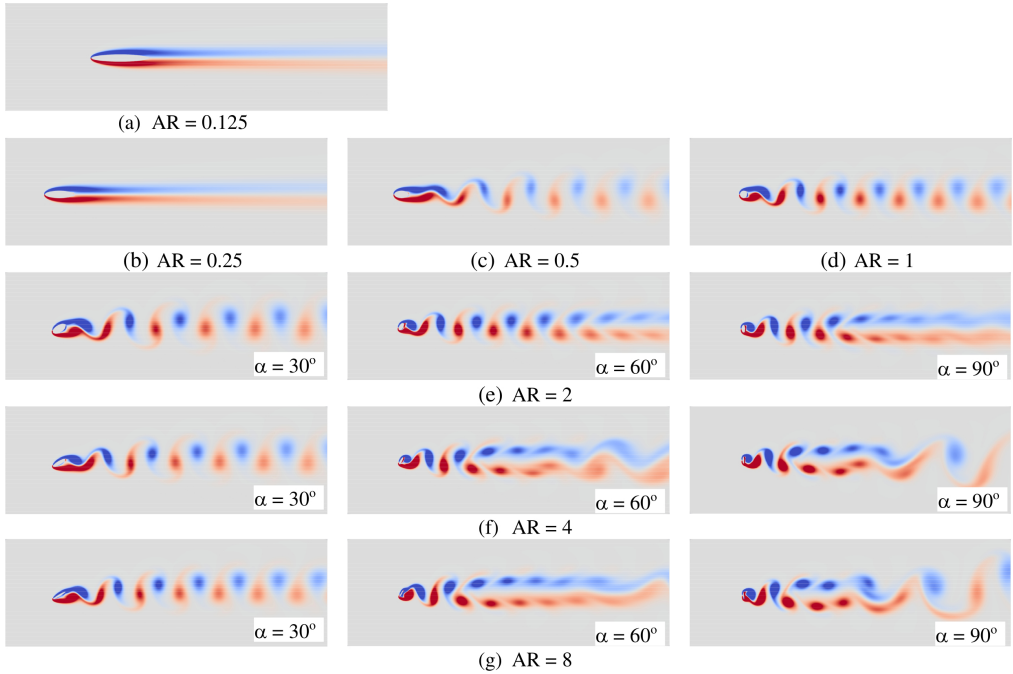


FIG. 12. Instantaneous distribution of the vorticity field of the flow around an elliptic cylinder with its various axis ratios (AR) and angles of attack (α) at $Re = 100$: (a) $AR = 0.125$, (b) $AR = 0.25$, (c) $AR = 0.5$, (d) $AR = 1$, (e) $AR = 2$, (f) $AR = 4$, and (g) $AR = 8$.

Figure 13 shows the time evolution of the drag coefficient (Cd) of the flow acting on an elliptic cylinder at $Re = 100$. For the axis ratio (AR) of 0.125 and 0.25, the steady symmetric vortex pair flow takes place; therefore, Cd remains unchanged. Moreover, Cd at $AR = 0.125$ is lower than that at $AR = 0.25$ due to a change in the viscous force component. For $AR = 0.5$ and 1, the vortex shedding happens, Cd fluctuates periodically, and its time-averaged value significantly increases, as shown in Fig. 13(a). This feature is the same as that at $Re = 65$. For $AR = 2, 4$, and 8 at $\alpha = 30^\circ$, as shown in Fig. 13(b), the Kármán vortex street is formed, and Cd at these AR drastically decreases, as compared to that at $AR = 1$, due to smoother streamlines of the flow surrounding the solid body. Cd slightly increases as AR rises from 2 to 8. For $AR = 2, 4$, and 8 at $\alpha = 60^\circ$, as indicated in Fig. 13(c), the wake pattern is Kármán wake followed by secondary wake. The maximal Cd belongs to that with $AR = 2$, followed by those at $AR = 8$ and 4. Compared to the circular cylinder, Cd at $AR = 2$ and $\alpha = 60^\circ$ is even higher. This indicates that the cylinder strongly resists the flow at this AR. Moreover, the fluctuation intensity of Cd at $\alpha = 60^\circ$ with $AR = 4$

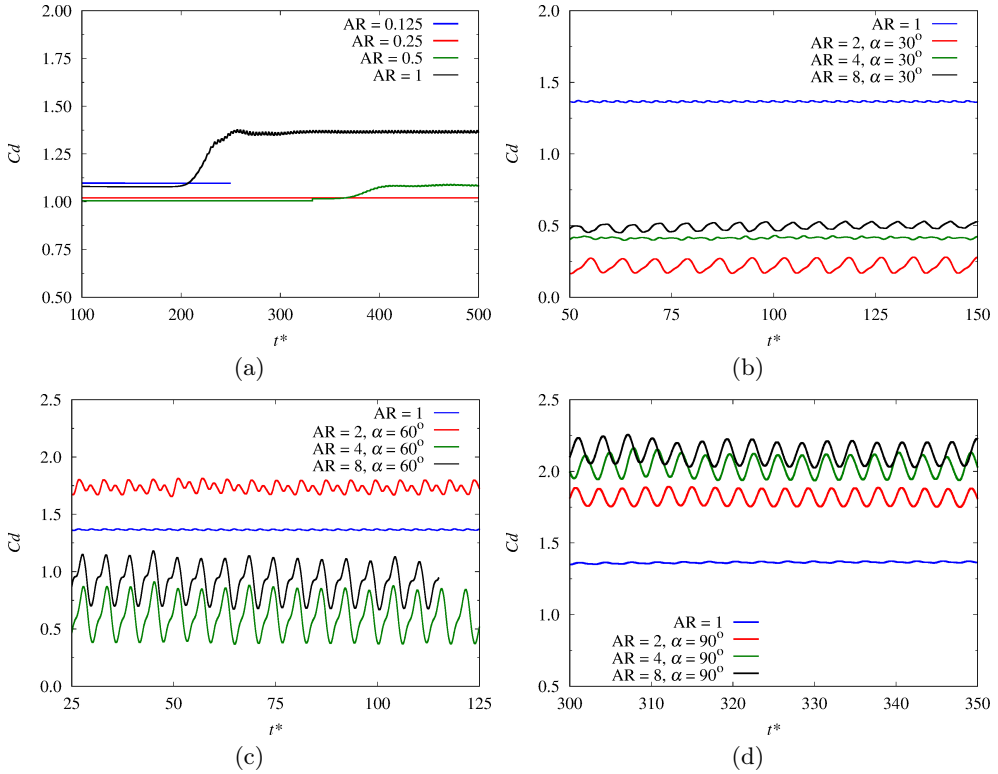


FIG. 13. Time evolution of drag coefficient (C_d) of the flow exerted on an elliptic cylinder with its various axis ratios (AR) and angles of attack (α) at $Re = 100$: (a) $AR = 0.125, 0.25, 0.5$ and 1 , (b) $AR = 2, 4$ and 8 at $\alpha = 30^\circ$, (c) $AR = 2, 4$ and 8 at $\alpha = 60^\circ$, and (d) $AR = 2, 4$ and 8 at $\alpha = 90^\circ$.

and 8 is higher than that in other cases at this Re . For $AR = 2, 4$, and 8 at $\alpha = 90^\circ$, as shown in Fig. 13(d), C_d s at these AR are higher than at $AR = 1$, and they significantly fluctuate.

3.5. Chaotic flow

Figure 14 shows an instantaneous distribution of the vorticity field of the flow around an elliptic cylinder at $Re = 150$. The steady symmetric vortex pair flow is observed at the axis ratio of $AR = 0.125$, as further clarified in plots of streamline shown in Fig. 10(c). The Kármán vortex street is formed behind the cylinder at $AR = 0.25, 0.5, 1$ and $AR = 2, 4, 8$ with $\alpha = 30^\circ$. For $AR = 2$ with $\alpha = 60^\circ$, as seen in Fig. 14(e), the Kármán wake followed by secondary wake takes place. For the rest cases, $AR = 2$ with $\alpha = 90^\circ$, $AR = 4, 8$ with $\alpha = 60^\circ, 90^\circ$, the chaotic flow is observed. In this flow pattern, the vortices are shed from both sides of the

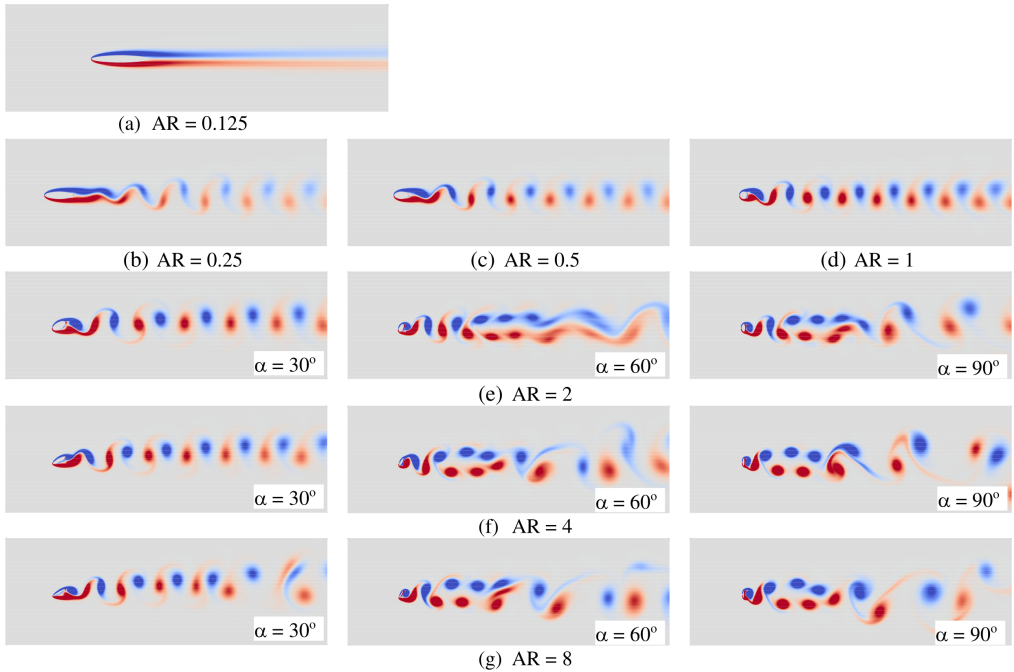


FIG. 14. Instantaneous distribution of the vorticity field of the flow around an elliptic cylinder with its various axis ratios (AR) and α at $Re = 150$: (a) $AR = 0.125$, (b) $AR = 0.25$, (c) $AR = 0.5$, (d) $AR = 1$, (e) $AR = 2$, (f) $AR = 4$, and (g) $AR = 8$.

cylinder and form a Kármán vortex street. However, this vortex street is rapidly distorted. Downstream, the counter-rotating vortices are paired, and they do not distribute in an orderly manner.

Figure 15 describes the time evolution of the drag coefficient (Cd) of the flow acting on an elliptic cylinder at $Re = 150$. For $AR = 0.125$, as seen in Fig. 15(a), Cd is constant with time because of steady symmetric vortex pair flow. For $AR = 0.25, 0.5$, and 1 , Cd starts to fluctuate periodically at $t^* = 200$ for $AR = 1$, $t^* = 250$ for $AR = 0.5$, and $t^* = 600$ for $AR = 0.25$ due to the appearance of the Kármán vortex street. It is clear that the flow is more stable and the fluctuation amplitude of Cd is lower at a lower AR.

For $AR = 2, 4$, and 8 with $\alpha = 30^\circ$, as seen in Fig. 15(b), the Kármán vortex street is also observed behind the cylinder, and the periodical vortex shedding occurs in the early stage of the flow. Cd is also less than that at $AR = 1$; however, its oscillation amplitude significantly increases. For $AR = 2$ with $\alpha = 60^\circ$, as seen in Fig. 15(c), the flow pattern is Kármán wake followed by secondary wake, Cd fluctuates periodically, and its time-averaged value is greater than that at $AR = 1$.

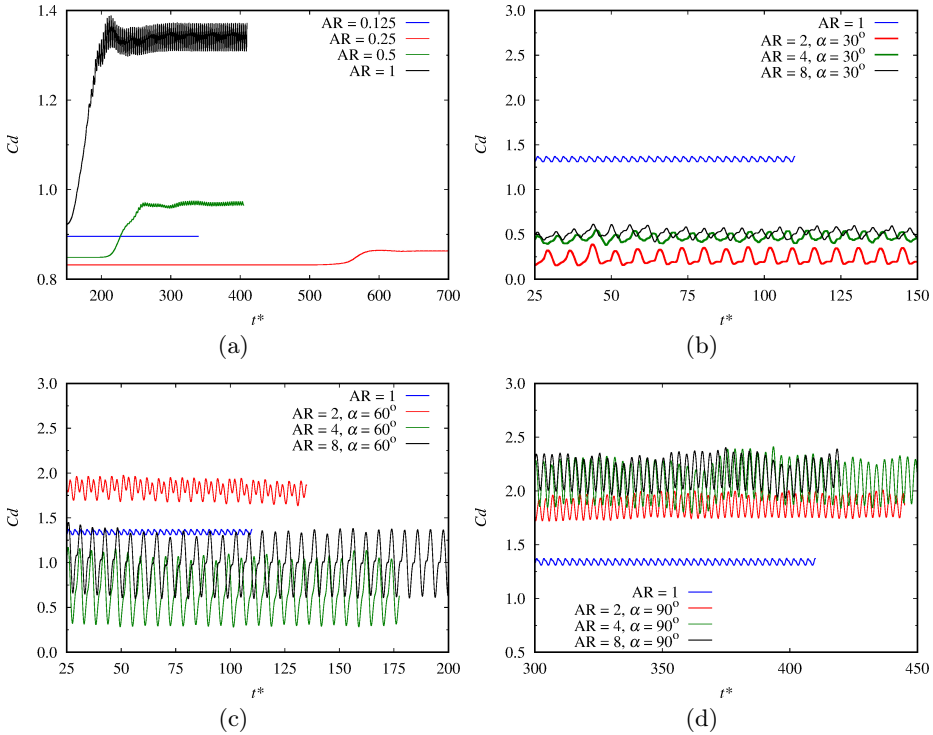


FIG. 15. Time evolution of the drag coefficient (C_d) of the flow exerted on an elliptic cylinder with its various axis ratios (AR) and α at $Re = 150$: (a) $AR = 0.125, 0.25, 0.5$, and 1 , (b) $AR = 2, 4$, and 8 at $\alpha = 30^\circ$, (c) $AR = 2, 4$, and 8 at $\alpha = 60^\circ$, (d) $AR = 2, 4$, and 8 at $\alpha = 90^\circ$.

For $AR = 4$ and 8 with $\alpha = 60^\circ$ and $AR = 2, 4, 8$ with $\alpha = 90^\circ$, as seen in Figs. 15(c) and 15(d), the chaotic flow is observed; C_d strongly fluctuates and is in nearly periodical behavior.

3.6. Flow characteristics

Figure 16 shows transition in the vortex wakes of the flow around an elliptic cylinder with various axis ratios (AR) at the angles of attack $\alpha = 30^\circ, 60^\circ$ and 90° and Re from 2 to 200 . As $Re, AR,$ and α vary, eight flow patterns, such as attached flow, steady symmetric vortex pair flow, steady asymmetric vortex flow, double-periodical vortex shedding, Kármán vortex street, Kármán wake followed by steady shear layers, Kármán wake followed by secondary wake, and chaotic flow, can take place. These flow patterns can be classified into steady flow composed of attached flow, steady symmetric vortex pair flow, and steady asymmetric vortex flow, and unsteady flow composed of Kármán vortex street, double-

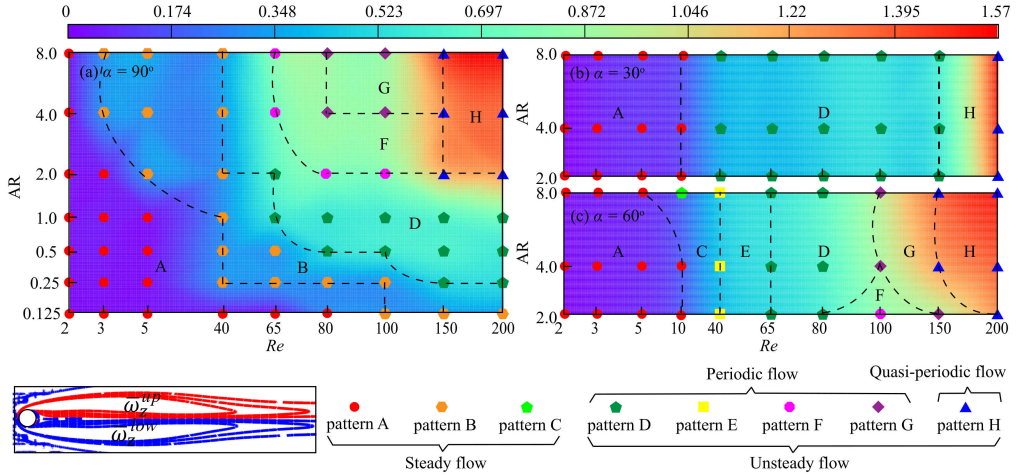


FIG. 16. Wake patterns of the flow around an elliptic cylinder at its angles of attack of $\alpha = 30^\circ, 60^\circ$ and 90° , where pattern A is attached flow, pattern B is steady symmetric vortex pair flow, pattern C is steady asymmetric vortex flow, pattern D is Kármán vortex street, pattern E is double-periodical vortex shedding, pattern F is Kármán wake followed by steady shear layers, pattern G is Kármán wake followed by secondary wake, and pattern H is chaotic flow. The transition of these flow patterns is identified using contours of $f(x, y) = \sum_{i=1}^{i=N_p} (|\omega_z^{\text{up}}| - |\omega_z^{\text{down}}|)$ computed using the vorticity flow surrounding the cylinder.

periodical vortex shedding, Kármán wake followed by steady shear layers, Kármán wake followed by secondary wake, and chaotic flow. Based on vortex shedding from the cylinder, the unsteady flows are characterized by two modes. The first mode, as observed in Kármán vortex street, double-periodical vortex shedding, Kármán wake followed by steady shear layers, is featured by the periodical oscillation of the lift coefficient Cl , while for the second one (chaotic flow), Cl has a quasi-periodical fluctuation.

At $\alpha = 90^\circ$, the attached flow is found at low Re for all axis ratios (AR). When AR decreases, the streamline is smoother, the flow is more stable, and this flow pattern can take place at a higher Re , as seen at $Re = 65$ for $AR = 0.125$. Similarly, the region of steady symmetric vortex pair flow is observed at a high Re or/and a low AR . For this investigated Re range, the Kármán vortex street is observed at $0.25 \leq AR \leq 2$ at $Re \geq 65$. The Kármán wake followed by secondary wake takes place at $65 \leq Re \leq 100$ and $AR \geq 2$. Meanwhile, the chaotic flow occurs at high $AR \geq 2$ and $Re \geq 150$. In particular, the double-periodical vortex shedding is not observed at this AoA.

At $\alpha = 30^\circ$ and 60° , the attached flow is only observed at Re from 2 to 5. From $Re \geq 40$, the flow is unsteady, and its wake pattern can be Kármán vortex street or Kármán wake followed by the secondary wake. The flow at $\alpha = 30^\circ$ is more

stable than that at $\alpha = 60^\circ$. The Kármán vortex street pattern can be observed at Re until 150 before turning into the chaotic flow. The Kármán wake followed by the secondary wake happens at $\alpha = 60^\circ$, while it is not found at $\alpha = 30^\circ$. The steady symmetric vortex pair cannot occur at these angles of attack. However, it is predicted that the steady flow with a single or two vortices attached behind the cylinder occurs at Re from 5 to 40. Furthermore, the contours of the $f(x, y)$ defined in the caption of Fig. 16 were used to determine the flow pattern regions. The blue and light-blue regions of the map indicate the steady flow mode, the red zone represents the quasi-periodic flow mode, and the rest of the map represents the periodic flow mode. These modes transition through a jump of $f(x, y)$.

Figure 17 shows the spatial structures of the flow wake around an elliptic cylinder using plots of modes generated by the proper orthogonal decomposition of the vorticity fluctuation. For the simulation case of $Re = 40$ and $AR = 0.5$, the steady symmetric vortex pair flow pattern is observed. The first three mode pairs play the most crucial roles in the partial structures of this wake. These mode pairs contribute 95% of the flow energy, in which the first mode pair (modes 1 and 2) occupies 70%, while the second (modes 3 and 4) and third (modes 5 and 6) pairs hold 18% and 7%, respectively. These modes are composed of the horizontal-axis-symmetrical opposite-signed pairs of the spatial deterministic structures. Besides, three spatially opposite-signed structure pairs represent the appearance of small and large vortex pairs behind the cylinder.

For the case of $Re = 40$, $AR = 8$, and $AoA = 60^\circ$, the double periodical vortex shedding pattern occurs, where the vortex wake behind the cylinder is similar to the Kármán vortex street. However, two vortex shedding frequencies are observed at this flow pattern. The first three mode pairs contribute 76% of the flow energy, in which the first mode pair carries out 35%, while the second and third mode pairs stand for 29% and 7%, respectively. The first mode pair (modes 1 and 2) shows the horizontal-axis-symmetrical like-signed spatial structures in the region near the cylinder. These spatial structures correspond to the Kármán vortices. However, these structures transition in the middle region downstream, and they are nearly switched to the horizontal-axis-symmetrical opposite-signed one far from the cylinder to represent small-scale instability inside the flow. The second mode pair (modes 3 and 4) with larger-scale spatial structures is symmetrical in the same sign with respect to the horizontal axis in the region far from the cylinder. The third mode pair indicates the existence of large-scale instability inside the flow.

For the case of $Re = 65$, $AR = 8$, and $AoA = 90^\circ$, the Kármán wake followed by steady shear layers appears behind the cylinder. The first three mode pairs correspond to 97% of the flow energy, and the remaining energy is distributed among higher-order modes. The spatial structures near the cylinder are similar to those at $Re = 40$, $AR = 8$, and $AoA = 60^\circ$, corresponding to the Kármán

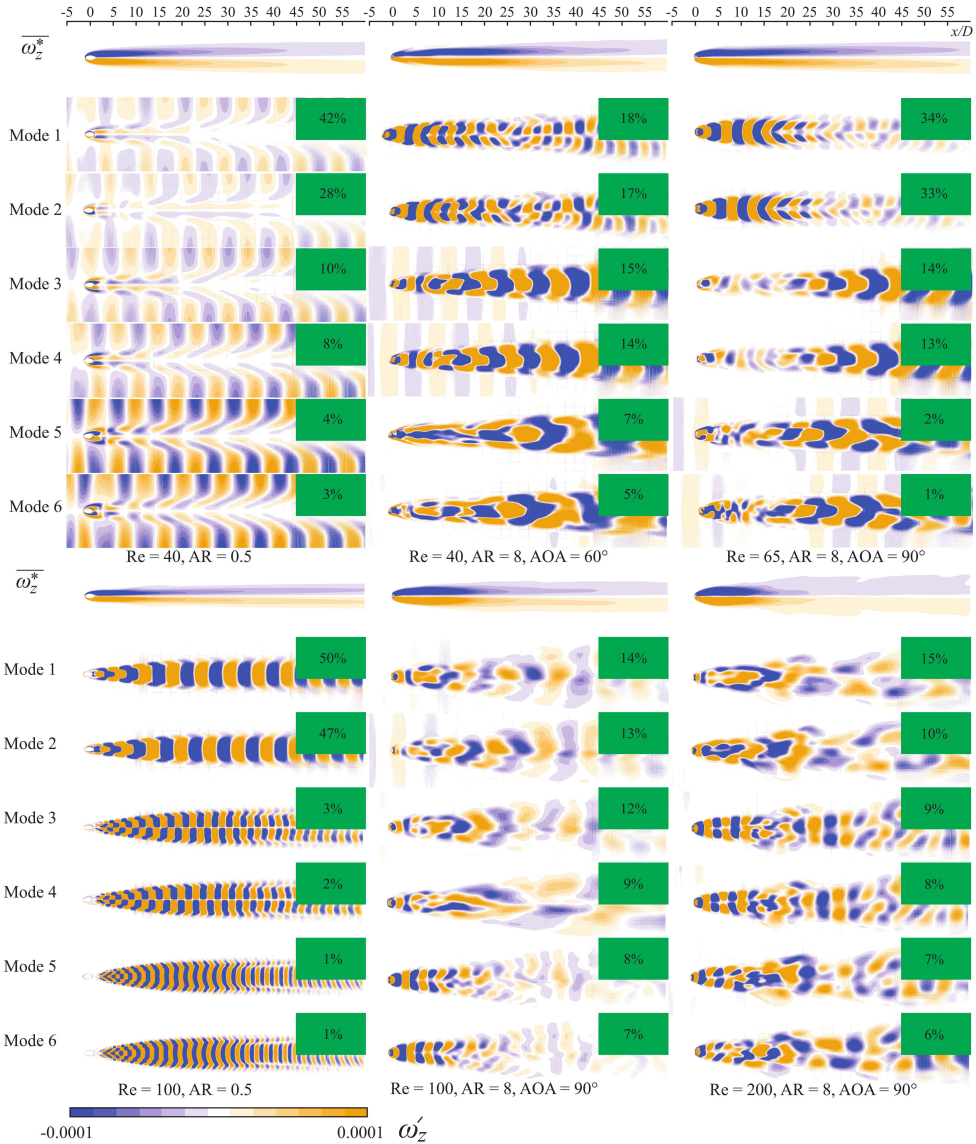


FIG. 17. The POD results for flow patterns. The top plots are the time-averaged vorticity contour $\overline{\omega}_z^*$. The remainder plots are spatial structures of fluctuating vorticity (ω'_z) of POD modes. The contours of POD modes' fluctuating vorticity are represented by the color bar. Steady symmetric vortex pair flow (Re = 40, AR = 0.5); double-periodical vortex shedding (Re = 40, AR = 8, AoA = 90°); Kármán wake followed by steady shear layers (Re = 65, AR = 8, AoA = 90°); Kármán vortex street (Re = 100, AR = 0.5); Kármán wake followed by a secondary wake (Re = 100, AR = 8, AoA = 90°); and chaotic flow (Re = 200, AR = 8, AoA = 90°).

vortices. Moreover, these spatial structures lose their symmetry in the region far from the cylinder due to the deformation of vortices. The second mode pair shows the large spatial structures of the flow far downstream. These structures are in the same sign symmetric with respect to the horizontal axis due to the decay of vortices and their merging into larger-scale shear layers. The third mode pair contributes slightly to the total energy of flow, and its asymmetry is explained as a result of instability inside the flow.

At $Re = 100$ and $AR = 0.5$, the first mode pair of spatial structures corresponds to 97% of the flow energy, characterized by symmetric spatial deterministic structures with the same sign across the horizontal axis. These structures are associated with the Kármán vortices and play a crucial role in the flow pattern. The second mode pair exhibits spatial structures that are symmetric with respect to the horizontal axis but in the opposite direction. This mode pair signifies a slight flow instability.

The Kármán wake followed by a secondary wake takes place at $Re = 100$, $AR = 8$, and $AoA = 90^\circ$. The first three mode pairs present 63% of the flow energy, in which the first mode pair corresponds to 27% while the second and third mode pairs lay on 21% and 15%, respectively. The first mode pair shows the distortion of the horizontal-axis-symmetrical like-signed spatial structure pairs, which represents the distorted Kármán vortex wake in the middle domain. Meanwhile, the second mode pair expresses the large-scale vortex structures far downstream, formed due to convection instability and the formation of the secondary vortex street. The third mode pair with the same-signed spatial structures symmetric with respect to the horizontal axis indicates the Kármán vortices near the cylinder.

At $Re = 200$, $AR = 8$ and $AoA = 90^\circ$, the chaotic flow takes place. The first three mode pairs contribute 55% of the flow energy, in which the first and third mode pairs characterize the chaotic flow structures. The spatial structures in the first and third mode pairs are not symmetric concerning the horizontal line. These pairs represent the small- and large-scale instabilities, and they play the main role in the flow. Meanwhile, the second mode pair with like-signed symmetric spatial pairs in the region near the cylinder represents the Kármán vortices. This mode pair contributes 17% of the flow energy.

The time-averaged drag (Cda) and the Strouhal number (St) of the flow around an elliptic cylinder at different axis ratios (AR), angles of attack α and Re are shown in Fig. 18. The Cda of the cylinder is generally lowest at $\alpha = 30^\circ$, followed by that at $\alpha = 60^\circ$ and $\alpha = 90^\circ$, for whole AR and Re . The smoothness of the streamline at a lower α explains this behavior. At low Re , when the viscous fluid force is significant, Cda for three angles of attack (α) is significant. Moreover, Cda for the cylinder with a smaller AR is higher due to a greater friction between the fluid and the cylinder surface. For $\alpha = 30^\circ$ and $\alpha = 60^\circ$,

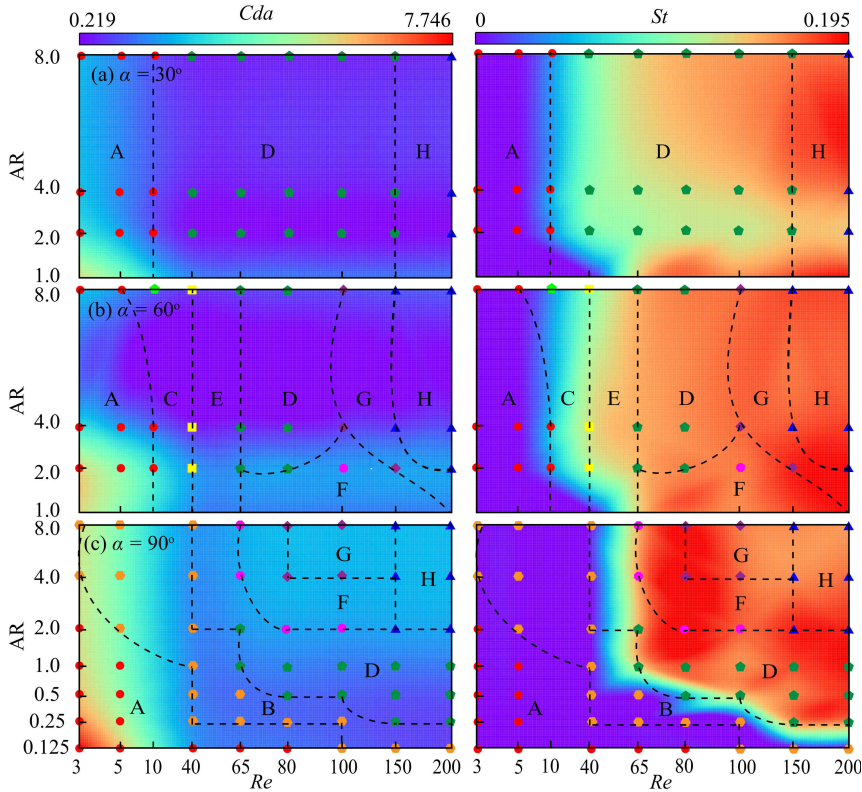


FIG. 18. Time-averaged drag coefficient (C_{da}) and the Strouhal number (St) of the flow around an elliptic cylinder with various axis ratios (AR), Re at the angles of attack $\alpha = 30^\circ, 60^\circ$ and 90° .

the vortex shedding of the flow develops at $Re = 40$, but it appears at $Re = 65$ for $\alpha = 90^\circ$. This is because when the cylinders are inclined horizontally, the flow loses its symmetry, which promotes the separation of the boundary layer and then rolling up to create vortices. As Re grows, St progressively increases for $\alpha = 30^\circ$ and $\alpha = 60^\circ$. Meanwhile, St at $\alpha = 90^\circ$ exhibits a high value when the vortex shedding takes place. We also observe the vortex shedding does not occur at high Re for low axis ratios ($AR \leq 1$), especially, for $Re = 200$ and $AR = 0.125$.

Figure 19 shows the root mean square (rms) of C'_D and C'_L of the flow exerted on an elliptic cylinder at various axis ratios (AR), angles of attack α , and Re . For $\alpha = 30^\circ$, the rms of C'_D is trivial for whole AR and α . However, the rms of C'_L is remarkable when $Re \geq 65$ and $AR \geq 4$, at which the Kármán vortex street pattern is observed. For $\alpha = 60^\circ$, the rms of C'_D shows the highest value in the ranges of $Re \geq 100$ and $AR \geq 4$, at which the chaotic flow takes place. The rms

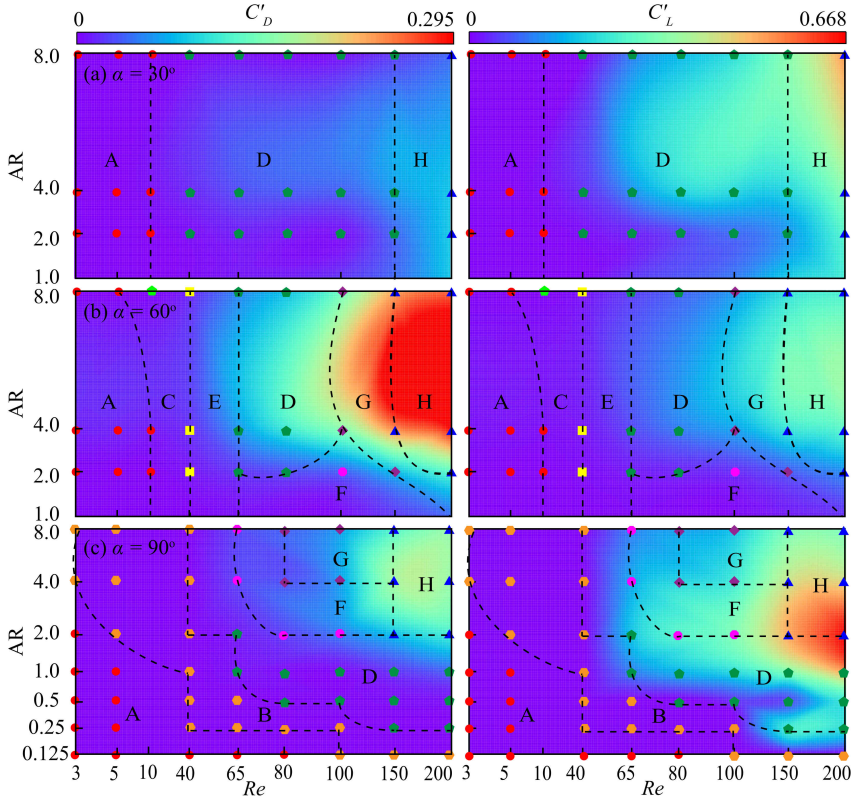


FIG. 19. Root mean square (rms) of C'_D and C'_L of the flow exerted on an elliptic cylinder with various axis ratios (AR), Re, and angles of attack (α), where $C'_D = Cd - Cda$ and $C'_L = Cl - Cla$.

of C'_L also exhibits a significant fluctuation in these ranges of AR and Re. The chaotic flow results in a high fluctuation of the drag Cd and lift Cl coefficients. Similarly, for $\alpha = 90^\circ$, the rms of C'_D and C'_L are remarkable in the ranges of $AR \geq 2$ and $Re \geq 100$, at which the chaotic flow takes place.

4. Conclusions

Transition in the vortex wakes of the flow around an elliptic cylinder was numerically investigated at Re from 3 to 200 using the vortex particle method. The axis ratio (AR) of the cylinder varies from 0.125 to 8, while its angle of attack (AoA) is examined at $\alpha = 30^\circ, 60^\circ$ and 90° . The remarkable findings of the characteristics of vortex wake behind an elliptic cylinder are presented as follows:

Eight vortex wake patterns, including attached flow, steady symmetric vortex flow, steady asymmetric vortex flow, Kármán vortex street, double-periodical

vortex shedding, Kármán wake followed by steady shear layers, Kármán wake followed by a secondary wake, and chaotic flow, can take place as a flow passes over an elliptic cylinder. The formation of these flow patterns significantly depends upon AR, AoA, and Re. They can be classified into steady and unsteady flows, in which the unsteady one is further characterized by periodic and quasi-periodic fluctuations.

For AoA = 90°, the attached flow is observed at low Re. As Re or/and AR increase, this flow pattern is switched into the steady symmetric vortex pair flow. With a further increase in Re, the Kármán vortex street takes place behind the cylinder. This wake pattern can be changed into the Kármán wake followed by steady shear layers or the Kármán wake followed by a secondary wake as AR rises. Specifically, when Re is further increased, the chaotic flow occurs. For AoA = 30°, the attached flow is directly switched into the Kármán vortex street as Re increases before turning into the chaotic flow at a higher Re. However, for AoA = 60°, we observed the steady asymmetric vortex flow at a low Re and the double-periodical vortex shedding flow at a higher Re. At a still higher Re, the Kármán vortices merge into the shear layers far downstream. These shear layers can roll up to form a secondary vortex street due to convection instability.

The drag coefficient is extremely high at low Re due to viscosity effects. As Re increases, the drag coefficient decreases. However, it remarkably rises as the vortex shedding occurs at a higher Re. The drag coefficient at AoA = 90° is higher than those at AoA = 30° and 60° because of a greater resistance of the flow at a higher AoA. The vortex shedding frequency is large as $Re \geq 65$ and $AR \geq 0.25$ for three AoA of 30°, 60° and 90°. The rms of C'_D is high when the chaotic flow takes place, and the greatest value is observed at AoA = 60°. Meanwhile, the rms of C'_L is considerable when the vortex shedding appears, and the cylinder at AoA = 90° induces C'_L higher than at AoA = 30° and 60°.

The spatial structures of the vortex wake behind the cylinder are analyzed using the proper orthogonal decomposition of the vorticity fluctuation. The steady shear layers and the Kármán vortices are represented by the horizontal-axis-symmetrical like-signed spatial structures. The spatial structures of the double periodical vortex shedding pattern are different from the Kármán vortex street. Both small- and large-scale instabilities exist significantly in the double periodical vortex shedding pattern, while they are trivial in the Kármán wake. The Kármán wake followed by a secondary wake is composed of symmetric, like-signed spatial structures near the cylinder and distorted ones far downstream. Meanwhile, the chaotic flow contains the asymmetric spatial structures with various scales and the symmetric like-signed spatial structure pairs near the cylinder. The large-scale asymmetric spatial structures contribute the most energy for this flow wake.

Acknowledgements

This research is funded by the Vietnam National Foundation for Science and Technology Development (NAFOSTED) under the grant number 107.03-2021.27.

Conflict of interest

The authors declare that they have no conflict of interest.

References

1. Z. FARUQUEE, D.S.K. TING, A. FARTAJ, R.M. BARRON, R. CARRIVEAU, *The effects of axis ratio on laminar fluid flow around an elliptical cylinder*, International Journal of Heat and Fluid Flow, **28**, 5, 1178–1189, 2007.
2. X. SHI, M. ALAM, H. BAI, *Wakes of elliptical cylinders at low Reynolds number*, International Journal of Heat and Fluid Flow, **82**, 108553, 2020.
3. J.H. LIENHARD, *Synopsis of Lift, Drag, and Vortex Frequency Data for Rigid Circular Cylinders*, Technical Extension Service, Washington State University, 1966.
4. D. BARKLEY, R.D. HENDERSON, *Three-dimensional Floquet stability analysis of the wake of a circular cylinder*, Journal of Fluid Mechanics, **322**, 215–241, 1996.
5. M. BREUER, J. BERNSDORF, T. ZEISER, F. DURST, *Accurate computations of the laminar flow past a square cylinder based on two different methods: lattice-Boltzmann and finite-volume*, International Journal of Heat and Fluid Flow, **21**, 2, 186–196, 2000.
6. W. HANKE, M. WITTE, L. MIERSCH, M. BREDE, J. OEFFNER, M. MICHAEL, F. HANKE, A. LEDER, G. DEHNHARDT, *Harbor seal vibrissa morphology suppresses vortex-induced vibrations*, Journal of Experimental Biology, **213**, 15, 2665–2672, 2010.
7. W.A. KHAN, R.J. CULHAM, M.M. YOVANOVICH, *Fluid flow around and heat transfer from elliptical cylinders: analytical approach*, Journal of Thermophysics and Heat Transfer, **19**, 2, 178–185, 2005.
8. H. HASIMOTO, *On the flow of a viscous fluid past an inclined elliptic cylinder at small Reynolds numbers*, Journal of Physical Society of Japan, **8**, 653–661, 1953.
9. S. KAZUHITO, U. AKIRA, T. AKIRA, *Low-Reynolds-number flow past an elliptic cylinder*, Journal of Fluid Mechanics, **136**, 277–289, 1983.
10. S.A. JOHNSON, M.C. THOMPSON, K. HOURIGAN, *Flow past elliptical cylinders at low Reynolds numbers*, 14th Australasian Fluid Mechanics Conference Adelaide University, Adelaide, Australia, 10–14, 2001.
11. S.A. JOHNSON, M.C. THOMPSON, K. HOURIGAN, *Predicted low frequency structures in the wake of elliptical cylinders*, European Journal of Mechanics – B/Fluids, **23**, 1, 229–239, 2004.
12. S.C.R. DENNIS, P.J.S. YOUNG, *Steady flow past an elliptic cylinder inclined to the stream*, Journal of Engineering Mathematics, **47**, 101–120, 2003.

13. H.S. YOON, J. YIN, C. CHOI, S. BALACHANDAR, M.Y. HA, *From the circular cylinder to the flat plate wake: the variation of Strouhal number with Reynolds number for elliptical cylinders*, Progress in Computational Fluid Dynamics, an International Journal, **16**, 3, 163–178, 2016.
14. I. PAUL, K.A. PRAKASH, S. VENGADESAN, *Onset of laminar separation and vortex shedding in flow past unconfined elliptic cylinders*, Physics of Fluids, **26**, 2, 023601, 2014.
15. G.-H. COTTET, P.D. KOUMOUTSAKOS, *Vortex Methods: Theory and Practice*, Cambridge University Press, 2000.
16. J.H. WALTHER, P. KOUMOUTSAKOS, *Three-dimensional vortex methods for particle-laden flows with two-way coupling*, Journal of Computational Physics, **167**, 1, 39–71, 2001.
17. F. NOCA, D. SHIELS, D. JEON, *A comparison of methods for evaluating time-dependent fluid dynamic forces on bodies, using only velocity fields and their derivatives*, Journal of Fluids and Structures, **13**, 15, 551–578, 1999.
18. V.L. NGUYEN, T. NGUYEN-THOI, V.D. DUONG, *Characteristics of the flow around four cylinders of various shapes*, Ocean Engineering, **238**, 109690, 2021.
19. B. SHARMAN, F.S. LIEN, L. DAVIDSON, C. NORBERG, *Numerical predictions of low Reynolds number flows over two tandem circular cylinders*, International Journal for Numerical Methods in Fluids, **47**, 5, 423–447, 2005.
20. H. DING, C. SHU, K.S. YEO, D. XU, *Numerical simulation of flows around two circular cylinders by mesh-free least square-based finite difference methods*, International Journal for Numerical Methods in Fluids, **53**, 2, 305–332, 2006.
21. J. CHOI, R.C. OBEROI, J.R. EDWARDS, J.A. ROSATI, *An immersed boundary method for complex incompressible flows*, Journal of Computational Physics, **224**, 2, 757–784, 2007.
22. A. HARICHANDAN, A. ROY, *Numerical investigation of low Reynolds number flow past two and three circular cylinders using unstructured grid CFR scheme*, International Journal of Heat and Fluid Flow, **31**, 2, 154–171, 2010.
23. K. SUPRADEEPAN, A. ROY, *Characterisation and analysis of flow over two side by side cylinders for different gaps at low Reynolds number: a numerical approach*, Physics of Fluids, **26**, 6, 063602, 2014.
24. C. MIMEAU, F. GALLIZIO, G.-H. COTTET, I. MORTAZAVI, *Vortex penalization method for bluff body flows*, International Journal of Numerical Methods in Fluids, **79**, 2, 55–83, 2015.
25. V.D. DUONG, V.D. NGUYEN, V.T. NGUYEN, I.L. NGO, *Low-Reynolds-number wake of three tandem elliptic cylinders*, Physics of Fluids, **34**, 4, 2022.
26. A.F. FIRDAUS, V.L. NGUYEN, L.R. ZUHAL, *Investigation of the flow around two tandem rotated square cylinders using the least square moving particle semi-implicit based on the vortex particle method*, Physics of Fluids, **35**, 2, 043605, 2023.

Received July 18, 2024; revised version August 28, 2024.

Published online November 19, 2024.